Annals of Biomedical Engineering, Vol. 47, No. 2, February 2019 (© 2018) pp. 425–438
https://doi.org/10.1007/s10439-018-02169-x

The Atheroprotective Nature of Helical Flow in Coronary Arteries

GIUSEPPE DE NISCO,[1] ANNETTE M. KOK,[2] CLAUDIO CHIASTRA,[3] DIEGO GALLO,[1] AYLA HOOGENDOORN,[2] FRANCESCO MIGLIAVACCA,[3] JOLANDA J. WENTZEL,[2] and UMBERTO MORBIDUCCI[1]

[1]PolitoBIOMed Lab, Department of Mechanical and Aerospace Engineering, Politecnico di Torino, Corso Duca degli Abruzzi, 24, 10129 Turin, Italy; [2]Department of Cardiology, Biomedical Engineering, Erasmus MC, Rotterdam, The Netherlands; and [3]Laboratory of Biological Structure Mechanics (LaBS), Department of Chemistry, Materials and Chemical Engineering "Giulio Natta", Politecnico di Milano, Milan, Italy

(*Received 17 August 2018; accepted 15 November 2018; published online 28 November 2018*)

Associate Editor Andreas Anayiotos oversaw the review of this article.

Abstract—Arterial hemodynamics is markedly characterized by the presence of helical flow patterns. Previous observations suggest that arterial helical blood flow is of physiological significance, and that its quantitative analysis holds promise for clinical applications. In particular, it has been reported that distinguishable helical flow patterns are potentially atheroprotective in the carotid bifurcation as they suppress flow disturbances. In this context, there is a knowledge gap about the physiological significance of helical flow in coronary arteries, a prominent site of atherosclerotic plaque formation. This study aimed at the quantitative assessment of helical blood flow in coronary arteries, and to investigate its possible associations with vascular geometry and with atherogenic wall shear stress (WSS) phenotypes in a representative sample of 30 swine coronary arteries. This study demonstrates that in coronary arteries: (1) the hemodynamics is characterized by counter-rotating bi-helical flow structures; (2) unfavorable conditions of WSS are strongly and inversely associated with helicity intensity ($r = -0.91$; $p < 0.001$), suggesting an atheroprotective role for helical flow in the coronary tree; (3) vascular torsion dictates helical flow features ($r = 0.64$; $p < 0.001$). The findings of this work support future studies on the role of helical flow in atherogenesis in coronary arteries.

Keywords—Helicity, Atherosclerosis, Computational fluid dynamics, Wall shear stress, Geometry.

INTRODUCTION

Early observations[15,31,34,58] using *in vitro* models suggested that arterial hemodynamics is markedly characterized by the presence of helical flow patterns. These *in vitro* data were confirmed *in vivo* using several different imaging modalities (as summarized in Table 1). As an example, a recent study using Color Duplex scanning observed in a cohort of 42 healthy volunteers that: (1) helical flow was present in 90% of the cases in the common carotid artery and the infrarenal aorta, and in 81% of the cases in the internal carotid artery; (2) 97% of the subjects had more sites with helical flow.[66] Furthermore, phase contrast magnetic resonance imaging (MRI) has allowed to highlight that the aortic hemodynamics is markedly characterized by the presence of helical flow patterns (Table 1). All those observations suggest that helical flow in arteries has a physiological significance, and that its quantitative analysis holds promise for clinical applications.[38]

The acknowledgment of a beneficial nature to helical flow in arteries is consistent with the fundamental role recognized for helicity in the organization/stabilization of both laminar and turbulent flows by the fluid mechanics theory.[44] In this regard, the onset of helical blood flow has been explained in terms of energy expenditure, i.e., distinguished helical blood flow patterns might be the consequence of an optimization in physiological transport process in the cardiovascular system, assuring an efficient perfusion as a result.[50,51] Furthermore, the forward-directed rotational fluid motion might stabilize blood flow, thereby minimizing flow disturbances and thus surface exposure to low and oscillatory wall shear stress (WSS), a condition which is known to influence endothelial function[65] creating a pro-atherogenic environment.[39] This last consideration motivated the investigation of the existence of a relationship between arterial helical flow and low and oscillatory WSS. For that purpose, in recent years hemodynamic indicators were introduced to enable the

Address correspondence to Umberto Morbiducci, PolitoBIOMed Lab, Department of Mechanical and Aerospace Engineering, Politecnico di Torino, Corso Duca degli Abruzzi, 24, 10129 Turin, Italy. Electronic mail: umberto.morbiducci@polito.it

TABLE 1. *In vivo* observations of helical blood flow patterns in arteries, using several imaging modalities.

Arterial segment	Imaging technique	References
	Aorta	
Thoracic aorta	Color Doppler ultrasound	Frazin *et al.*[15]
Thoracic aorta	4D phase contrast MRI	Kilner *et al.*[32]
Thoracic aorta	4D phase contrast MRI	Bogren and Buonocore[5]
Thoracic aorta	4D phase contrast MRI	Bogren *et al.*[7]
Thoracic aorta	4D phase contrast MRI	Houston *et al.*[29]
Thoracic aorta	4D phase contrast MRI	Bogren *et al.*[6]
Supra-renal aorta	MR angiography	Houston *et al.*[28]
Thoracic aorta	4D phase contrast MRI	Markl *et al.*[41]
Thoracic aorta	4D phase contrast MRI	Hope *et al.*[26]
Thoracic aorta	4D phase contrast MRI	Morbiducci *et al.*[50]
Ascending aorta	4D phase contrast MRI	Hope *et al.*[27]
Thoracic aorta	4D phase contrast MRI	Morbiducci *et al.*[51]
Thoracic aorta	4D phase contrast MRI	Bürk *et al.*[8]
Thoracic aorta	4D phase contrast MRI	Frydrychowicz *et al.*[16]
Thoracic aorta	4D phase contrast MRI	Geiger *et al.*[23]
Thoracic aorta	4D phase contrast MRI	Sigfridsson *et al.*[63]
Ascending aorta	Doppler ultrasound	Hansen *et al.*[24]
Infra-renal aorta	Color duplex scanning	Stonebridge *et al.*[66]
Thoracic aorta	4D phase contrast MRI	Arnold *et al.*[2]
Thoracic aorta	4D phase contrast MRI	Garcia *et al.*[22]
	Carotid arteries	
Carotid bifurcation	Ultrasound duplex scanning	Ku *et al.*[35]
Internal carotid artery	4D phase contrast MRI	Bammer *et al.*[4]
Internal carotid artery	4D phase contrast MRI	Wetzel *et al.*[71]
Internal carotid artery	4D phase contrast MRI	Markl *et al.*[42]
Common carotid artery	4D phase contrast MRI	Knobloch *et al.*[33]
External carotid artery	4D phase contrast MRI	Knobloch *et al.*[33]
Internal carotid artery	4D phase contrast MRI	Knobloch *et al.*[33]
Internal carotid artery	4D phase contrast MRI	Meckel *et al.*[43]
Common carotid artery	Color duplex scanning	Stonebridge *et al.*[66]
Internal carotid artery	Color duplex scanning	Stonebridge *et al.*[66]
	Pulmonary arteries	
Right pulmonary artery	4D phase contrast MRI	Bogren and Buonocore[5]
Right pulmonary artery	4D phase contrast MRI	François *et al.*[14]
Main pulmonary artery	4D phase contrast MRI	Bächler *et al.*[3]
Right Pulmonary artery	4D phase contrast MRI	Bächler et al.[3]
Main pulmonary artery	4D phase contrast MRI	Schäfer *et al.*[60]
Right pulmonary artery	4D phase contrast MRI	Schäfer *et al.*[60]
	Femoral arteries	
Femoral arteries	Color Doppler ultrasound	Stonebridge *et al.*[65]
Femoral arteries	4D phase contrast MRI	Frydrychowicz *et al.*[17]
Femoral arteries	Color duplex scanning	Stonebridge *et al.*[66]
	Iliac arteries	
Iliac arteries	4D phase contrast MRI	Frydrychowicz *et al.*[17]
	Intracranial arteries	
Basilar artery	4D phase contrast MRI	Bammer *et al.*[4]

quantitative analysis of helical blood flow patterns in arteries.[49] Findings in the human carotid bifurcation[19,20] and in the human aorta[48] showed that a high helical flow intensity suppresses flow disturbances, and thereby is potentially protective for atherosclerotic plaque build-up. Moreover, numerical studies suggested that helical flow influences transport and transfer of atherogenic particles to the vessel wall, ultimately contributing to the distribution of atherosclerotic plaques at the luminal surface.[36,37]

Until now, there is paucity of studies on the nature of helical blood flow patterns in coronary arteries. In this study we (1) assess the quantitative amount of helical blood flow, and (2) investigate if correlations exist among helical flow, vascular geometry and descriptors of disturbed shear stress in a representative sample of swine-specific computational hemodynamic

models of coronary arteries. The study aims at bridging the gap of knowledge still existing on the atheroprotective nature of helical flow in coronary arteries.[47]

MATERIALS AND METHODS

Animal Population and Imaging

Ten adult familial hypercholesterolemia Bretoncelles Meishan mini-pigs with a low-density lipoprotein receptor mutation were fed a high fat diet. For each animal model, the right (RCA), the left anterior descending (LAD), and the left circumflex (LCX) coronary artery were imaged at baseline using computed coronary tomography angiography (CCTA) and intravascular ultrasound (IVUS), as detailed in the Supplemental Methods. In each artery, blood flow velocity was measured at several locations with the ComboWire (Volcano Corp., Rancho Cardova, CA, USA).

Ethical approval was obtained to perform the pig study (EMC nr. 109-14-10) and the study was performed according to the National Institute of Health guide for the Care and Use of Laboratory animals.[54]

Geometry Reconstruction

The scheme applied for coronary arteries models reconstruction is summarized in Fig. 1. Technical details are presented in the Supplemental Methods (Fig. S.1). In short, IVUS images were segmented into lumen contours and stacked upon the 3D CCTA centerline. Additional luminal regions proximal to the IVUS segment up to the aorta and at least two diameters distal to the IVUS-based models were segmented using the CCTA images.[59]

The 30 reconstructed luminal surfaces of the coronary arteries (10 RCA, 10 LAD, and 10 LCX) are presented in Fig. 2. Computational hemodynamics was performed on all models including the side branches. However, data analysis was performed in the main branch of the RCA, LAD and LCX segments only. To do that, in the post-processing step side branches were removed using the open-source Vascular Modeling Toolkit (VMTK, http://www.vmtk.org/).

Morphometric Descriptors

A robust centerline-based analysis of coronary arteries geometry was applied (see Supplemental Methods), as proposed elsewhere.[20] In detail, here the average values of curvature ($\bar{\kappa}$) and torsion ($\bar{\tau}$) along the vessel were considered, which are known to have an influence on arterial hemodynamics.[20]

Computational Hemodynamics

The governing equations of fluid motion, the Navier–Stokes equations, were numerically solved in their discrete form by applying the finite volume method.

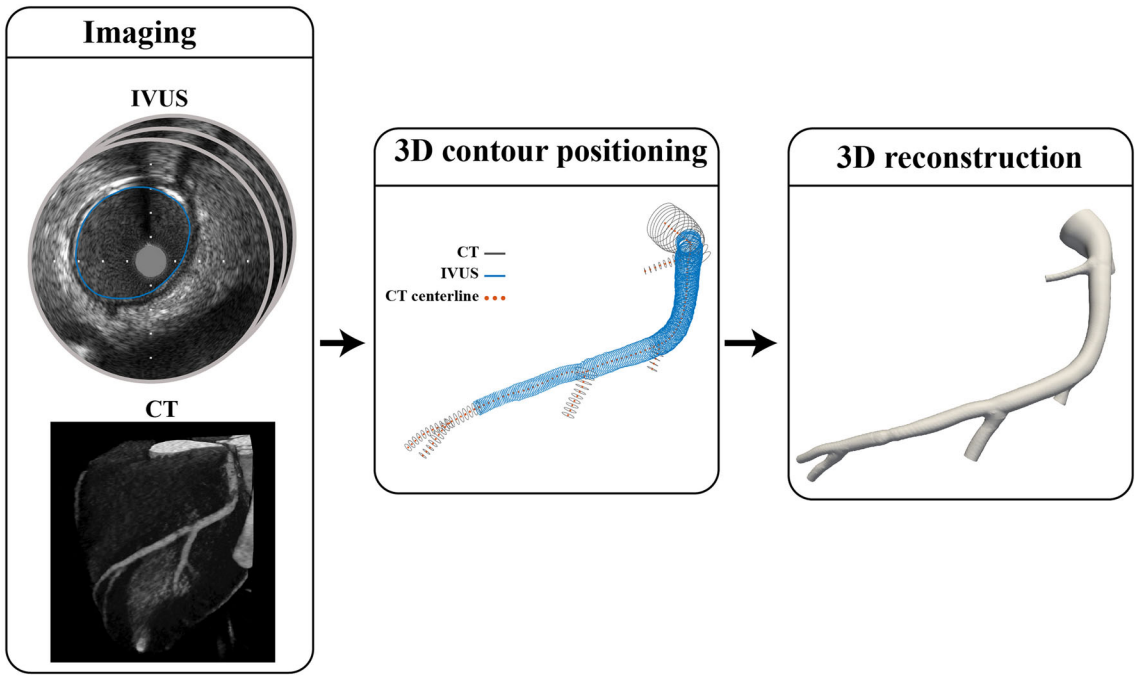

FIGURE 1. Scheme applied for swine coronary artery geometries reconstruction from CT and IVUS images.

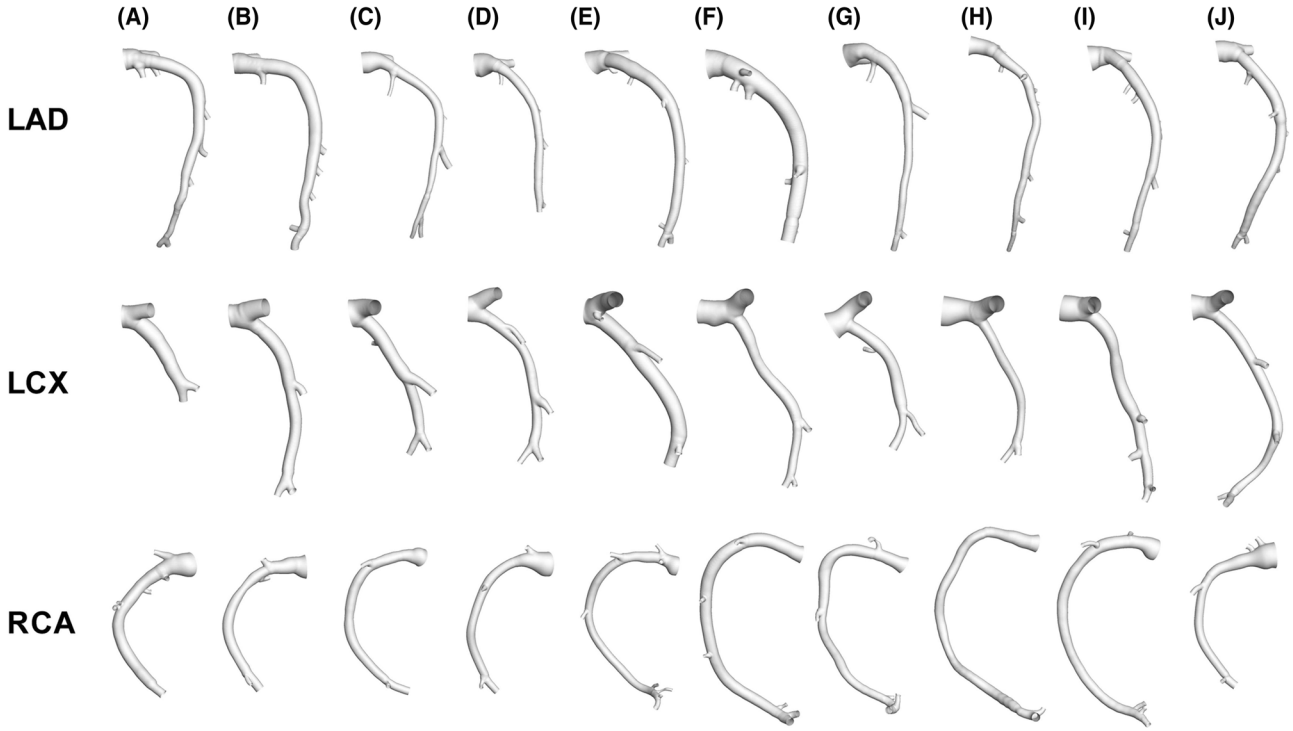

FIGURE 2. Geometry of the 30 swine coronary artery models. Labels from A to J identify the single swine model. For each swine, LAD, LCX and RCA geometries were reconstructed.

The adopted discretization schemes are detailed in the Supplemental Methods (an explanatory example of the applied mesh strategy is presented in Fig. S.2, Supplemental data). Blood was assumed as an incompressible, homogeneous fluid with density ρ equal to 1060 kg/m^3, and its non-Newtonian behavior was modeled assuming it as a Carreau fluid.[10,69] Arterial walls were assumed to be rigid with no-slip condition. The derivation of boundary conditions from *in vivo* Doppler velocity measurements adopted here represents an accurate method to obtain personalized coronary artery computational models.[62] Technically, in each artery the instantaneous maximum blood flow velocity was measured at several locations upstream and downstream of each side branch with the ComboWire. At each measurement site, maximum velocity data were used to estimate the flow rate as proposed elsewhere.[57] As condition at the inflow boundary, the most proximal measurement-based flow rate value was prescribed in terms of time-dependent flat velocity profile (Fig. S.3, Supplemental data). At each side branch a flow ratio was applied as outflow boundary, based on difference between upstream and downstream velocity-based flow rate measurements. In those vessel segments where velocity measurements were inaccurate or not available, the Huo-Kassab diameter-based scaling law[30] was used to estimate the flow ratio to be prescribed (an explanatory example of the applied boundary conditions is presented in Fig. S.4, Supplemental data).

Hemodynamic Descriptors

Helical flow in the 30 coronary artery models was characterized in terms of strength, size and relative rotational direction by applying different helicity-based descriptors, listed in Table 2. In detail, cycle-average helicity (h_1) and helicity intensity (h_2), signed (h_3) and unsigned helical rotation balance (h_4) were calculated as reported elsewhere.[19] Average helicity descriptors h_1 and h_2 indicate the net amount and the intensity of helical flow, respectively, while the helical rotation balance descriptors measure the prevalence (identified by the sign of descriptor h_3) or only the strength (h_4) of relative rotations of helical flow structures.

The luminal distribution of three ''established'' WSS-based descriptors, namely time-averaged wall shear stress (TAWSS), oscillatory shear index (OSI),[35] and relative residence time (RRT)[25] was computed (Table 3). Two ''emerging'' descriptors of WSS multidirectionality were also considered. The first is the transversal WSS (transWSS),[55] defined as the average WSS component acting orthogonal to the time-averaged WSS vector direction, and the second is its normalized version, the Cross Flow Index (CFI)[45]

TABLE 2. Definition of helicity-based intravascular hemodynamic descriptors.

Average helicity (h_1)	$h_1 = \frac{1}{TV}\int_T\int_V \mathbf{v}\cdot\boldsymbol{\omega} dV dt$
Average helicity intensity (h_2)	$h_2 = \frac{1}{TV}\int_T\int_V \lvert\mathbf{v}\cdot\boldsymbol{\omega}\rvert dV dt$
Signed balance of counter-rotating helical flow structures (h_3)	$h_3 = \frac{h_1}{h_2} \quad -1 \le h_3 \le 1$
Unsigned balance of counter-rotating helical flow structures (h_4)	$h_4 = \frac{\lvert h_1\rvert}{h_2} \quad 0 \le h_4 \le 1$

v is the velocity vector, ω is the vorticity vector; T is the period of the cardiac cycle; V is the arterial volume.

TABLE 3. Definition of WSS-based hemodynamic descriptors.

Time-averaged WSS (TAWSS)	$\mathrm{TAWSS} = \frac{1}{T}\int_0^T \lvert\mathbf{WSS}\rvert dt$
Oscillatory Shear Index (OSI)	$\mathrm{OSI} = 0.5\left[1 - \left(\frac{\left\lvert\int_0^T \mathbf{WSS} dt\right\rvert}{\int_0^T \lvert\mathbf{WSS}\rvert dt}\right)\right]$
Relative residence time (RRT)	$\mathrm{RRT} = \frac{1}{\mathrm{TAWSS}\cdot(1-2\cdot\mathrm{OSI})} = \frac{1}{\frac{1}{T}\left\lvert\int_0^T \mathbf{WSS} dt\right\rvert}$
Transverse wall shear stress (transWSS)	$\mathrm{transWSS} = \frac{1}{T}\int_0^T \left\lvert\mathbf{WSS}\cdot\left(\mathbf{n}\times\frac{\int_0^T \mathbf{WSS} dt}{\left\lvert\int_0^T \mathbf{WSS} dt\right\rvert}\right)\right\rvert dt$
Cross Flow Index (CFI)	$\mathrm{CFI} = \frac{1}{T}\int_0^T \left\lvert\frac{\mathbf{WSS}}{\lvert\mathbf{WSS}\rvert}\cdot\left(\mathbf{n}\times\frac{\int_0^T \mathbf{WSS} dt}{\left\lvert\int_0^T \mathbf{WSS} dt\right\rvert}\right)\right\rvert dt$

WSS is the WSS vector; T is the period of the cardiac cycle; **n** is the unit vector normal to the arterial surface at each element.

TABLE 4. Definition of local normalized helicity (LNH), and of the projections of WSS vector respectively along (1) the "axial direction" ($\mathbf{WSS}_{ax}$), identified as the direction of the tangent to the vessel's centerline, and (2) the secondary direction ($\mathbf{WSS}_{sc}$), orthogonal to the axial direction and related to secondary flow.

Local normalized helicity (LNH)	$\mathrm{LNH} = \frac{\boldsymbol{v}\cdot\boldsymbol{\omega}}{\lvert\boldsymbol{v}\rvert\cdot\lvert\boldsymbol{\omega}\rvert} = \cos\gamma$
Axial WSS ($\mathbf{WSS}_{ax}$)	$\mathbf{WSS}_{ax} = \frac{\mathbf{WSS}\cdot\mathbf{C}'}{\lvert\mathbf{C}'\rvert}\frac{\mathbf{C}'}{\lvert\mathbf{C}'\rvert}$
Secondary WSS ($\mathbf{WSS}_{sc}$)	$\mathbf{WSS}_{sc} = \frac{\mathbf{WSS}\cdot\mathbf{S}}{\lvert\mathbf{S}\rvert}\frac{\mathbf{S}}{\lvert\mathbf{S}\rvert}; \quad \mathbf{S} = \frac{\mathbf{C}'\times\mathbf{R}}{\lvert\lvert\mathbf{C}'\rvert\mathbf{R}\rvert}$

LNH, $\mathbf{WSS}_{ax}$, and $\mathbf{WSS}_{sc}$ are used here for visualization purposes. **v** is the velocity vector; ω is the vorticity vector; γ is the angle between the velocity and vorticity; **WSS** is the WSS vector; $\mathbf{C}'$ is the vector tangent to the centerline curve **C** at curvilinear abscissa *s;* **R** is the vector directed from the generic point at the arterial surface, lying on the vessel's cross section identified by $\mathbf{C}'$ at curvilinear abscissa *s,* and the point of application of $\mathbf{C}'$.

(Table 3). As in previous studies,[19,21] data from all simulations were pooled to define objective thresholds for 'disturbed shear stress'. From combined data, the lower tertile (i.e., the 33th percentile) for TAWSS, and the upper tertile (i.e., the 66th percentile) for OSI, RRT, transWSS, and CFI were identified. For each model, the percentage of surface area (SA) exposed to OSI, RRT, transWSS, and CFI values belonging to the upper (TAWSS lower) tertile was quantified. These areas were denoted as OSI66, RRT66, transWSS66, CFI66, and TAWSS33, respectively. Intravascular flow was investigated in terms of helical flow amount and topology.

The quantitative analysis, based on the hemodynamic descriptors in Tables 2 and 3, was substantiated by visualizations of near-wall and intravascular quantities. The normalized internal product between local velocity and vorticity vectors (Table 4), labeled as local normalized helicity (LNH),[49] was used to visualize helical blood flow inside the coronary segments. The LNH allows to visualize left- and right-handed fluid structures in arteries[19,48] and isosurfaces of cycle average LNH values were used throughout the

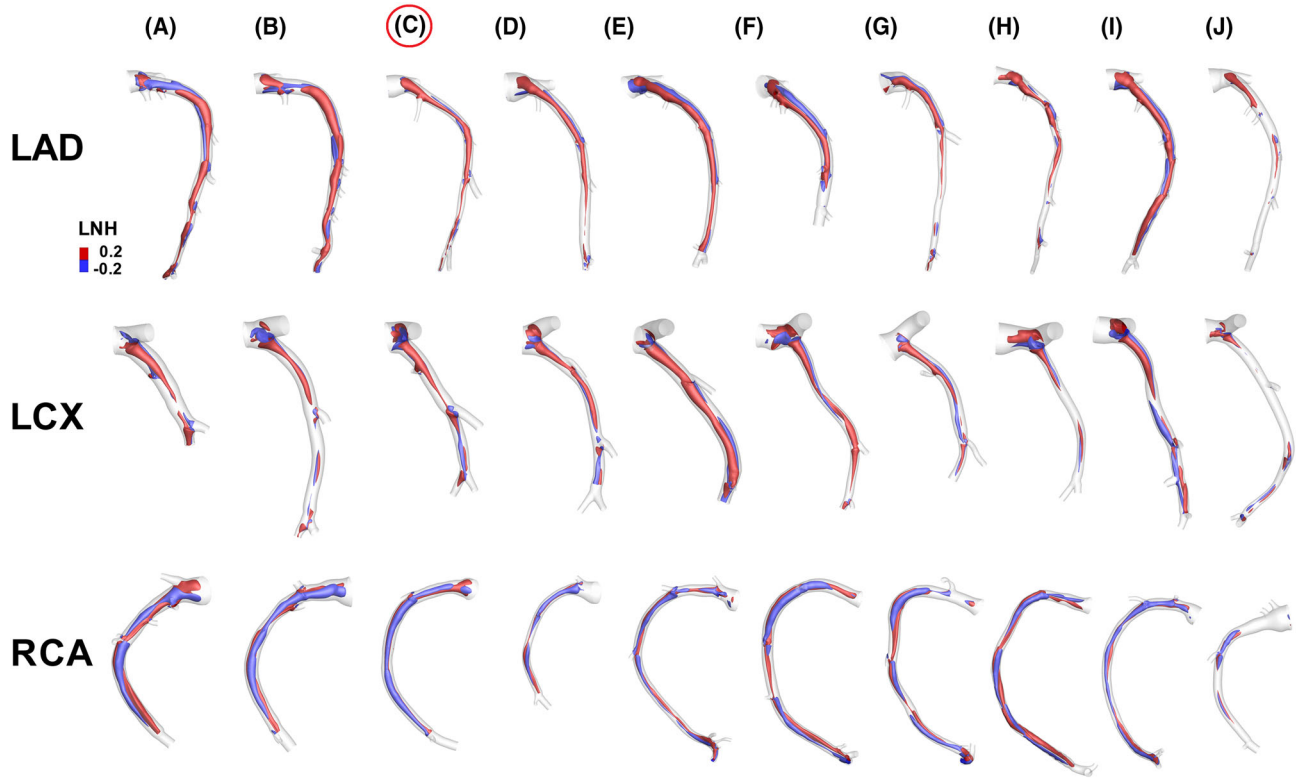

FIGURE 3. Intravascular fluid structures in the 30 coronary arteries. For each case, isosurfaces of cycle-average LNH (LNH = ± 0.2) are presented. Distinguishable left-handed (LNH < 0) and right-handed (LNH > 0) helical flow structures can be observed in all coronary arteries. Labels from A to J identify the single swine model. For each swine, LAD, LCX and RCA geometries were reconstructed.

manuscript. Moreover, two more descriptors visualizing WSS multidirectionality were evaluated considering the cycle-average values of the projections of WSS vector respectively along (1) the "axial direction" ($\mathbf{WSS}_{ax}$), identified as the direction of the tangent to the vessel's centerline, and (2) the secondary direction ($\mathbf{WSS}_{sc}$), orthogonal to the axial direction and related to secondary flow (Table 4).[46]

Statistical Analysis

Bivariate correlations among WSS-based, helicity-based and geometric descriptors were determined in Matlab environment (The MathWorks Inc., USA) by using Spearman rank ordering. Regression analysis was used to identify relationships between each pair of descriptors and reported as Spearman correlation coefficients. Significance was assumed for $p < 0.05$.

RESULTS

Helical blood flow patterns were visualized using the isosurface of cycle-average LNH, with blue and red colors indicating left-handed and right-handed helical flow rotation, respectively (Fig. 3). Notably, all 30 coronary artery models presented two distinguishable counter-rotating helical flow structures. It can be also appreciated that: (1) in most of the cases, counter-rotating cycle-average helical flow structures are distributed all along the length of the artery; (2) despite inter-individual variations, no marked differences among the coronary artery types is present.

Figure 4 shows for 3 different types of coronary arteries from animal model C (see Fig. 2) the visualizations of the LNH cycle-average isosurfaces, and the maps of the cycle-average secondary ($\mathbf{WSS}_{sc}$) and axial ($\mathbf{WSS}_{ax}$) WSS vector projections. As for LNH, also for the $\mathbf{WSS}_{sc}$ blue and red colors identify the left and right-handed direction, respectively. For $\mathbf{WSS}_{ax}$ the blue and red colors identify the backward and forward flow direction, respectively. Interestingly for the LAD and RCA there was a clear match between LNH and $\mathbf{WSS}_{sc}$ direction of rotation, however for the LCX this was less evident. Furthermore, Fig. 4 shows that $\mathbf{WSS}_{ax}$ is mainly positive, meaning that the WSS vector is predominantly aligned with the forward flow direction. Secondary and axial WSS distributions are presented in the supplemental Fig. S.5 for all the 30 coronary artery models. The results presented in

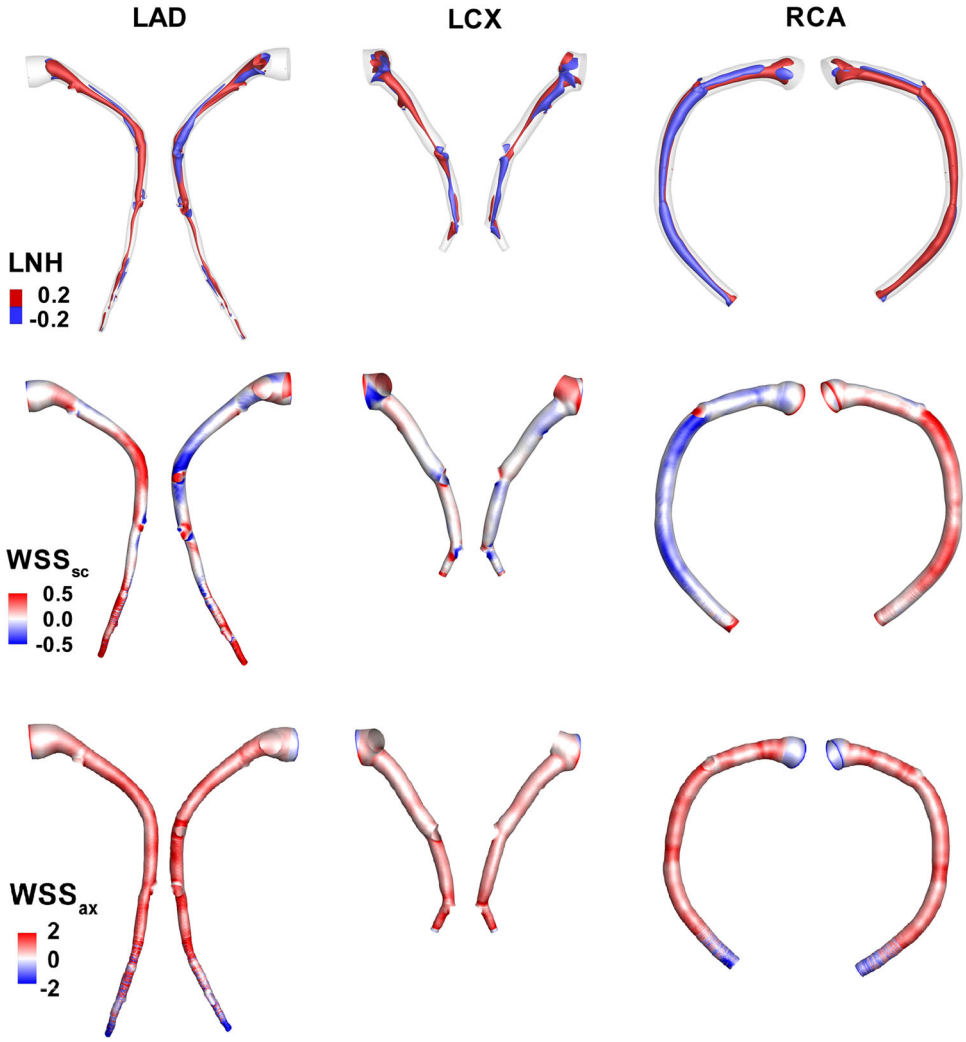

FIGURE 4. Visualization of LNH cycle-average isosurfaces, and of maps of cycle-average secondary (WSS_{sc}) and axial (WSS_{ax}) WSS vector projections for the three different types of coronary arteries (LAD, LCX, RCA) from the representative animal model C (see Fig. 2). As for LNH, also for the WSS_{sc} blue and red colors identify the left and right-handed direction, respectively. For WSS_{ax} the red and blue colors identify the forward and backward flow direction, respectively.

Figs. 4 and S.5 suggested that the bi-helical arrangement of intravascular blood flow delineates the near-wall hemodynamics of coronary arteries.

To complete the intra-individual analysis of representative animal model C, also the luminal distribution of the other computed WSS-based descriptors were presented in Fig. 5. Notably, OSI, transWSS and CFI values at the luminal surface were low, suggesting that WSS is scarcely multidirectional in the three different types of coronary arteries of animal C (Fig. S.6 and Table S.1, Supplemental data). Figure 5 highlights that the location of the low WSS regions in the coronary arteries was more focal in the LAD and RCA, but less in the LCX. Moreover, TAWSS and RRT showed a similar distribution, independent of coronary artery type, which was also the case for CFI and transWSS.

The visualization of SAs exposed to low WSS (TAWSS33) highlights wide inter-individual variations (Fig. 6). In some cases the luminal surface is largely exposed to low WSS (e.g., case J-LDA, case G-LCX, case E-RCA) whereas other arteries are hardly exposed (e.g., case I-LDA, case H-RCA). The distribution of SAs exposed to OSI66, RRT66, transWSS66, CFI66 for all the 30 coronary artery models is presented in the Supplemental data (Fig. S.7).

The correlation coefficients between each possible couple of disturbed shear stress and geometry descriptors are summarized in Table 5. The WSS-based percentage SAs (exposed to) were significantly correlated to each other, with the sole exception of OSI66 and RRT66.

In this study, RRT66 was considered to be equivalent to TAWSS33. This consideration was based on the

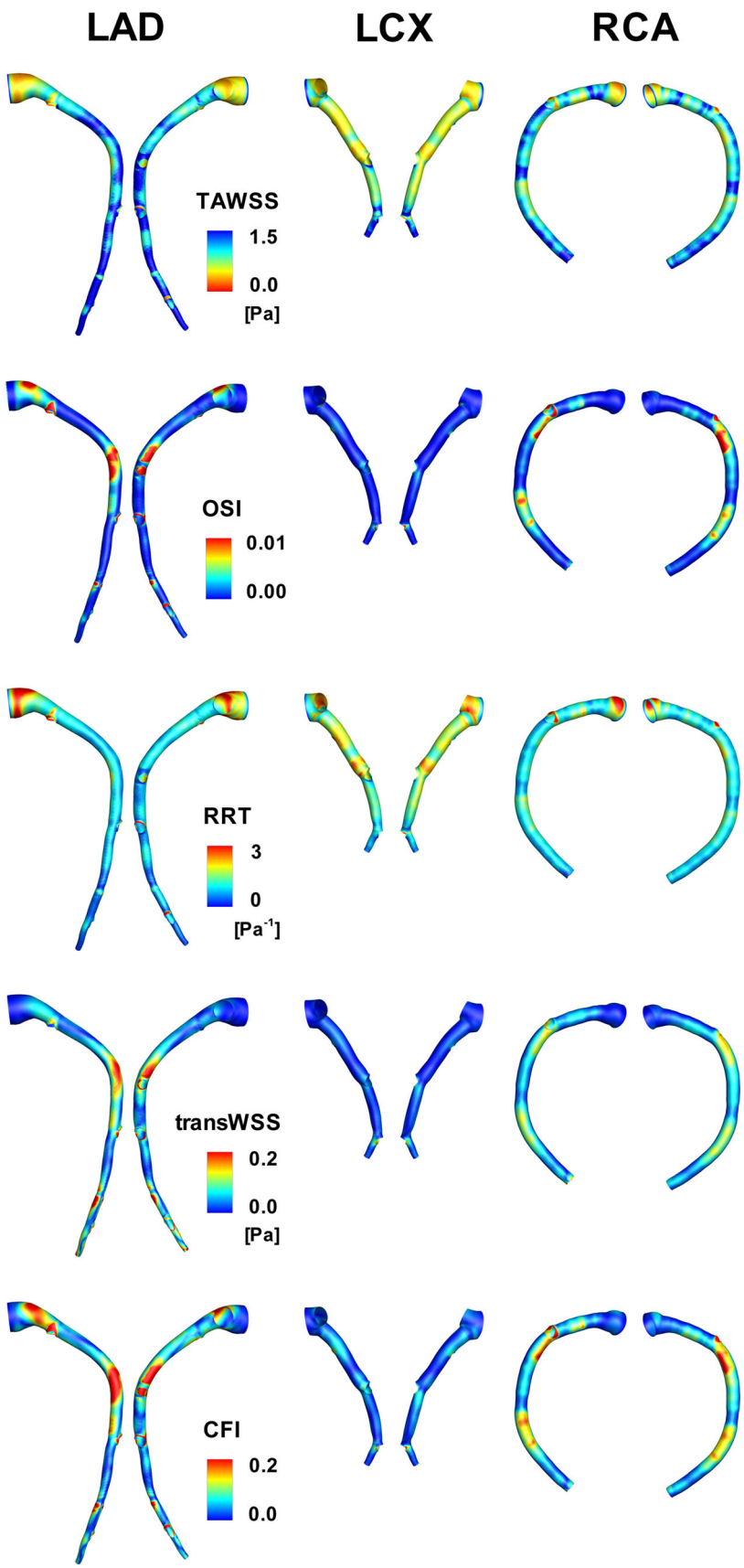
LAD
LCX
RCA
TAWSS
1.5
0.0
[Pa]
OSI
0.01
0.00
RRT
3
0
[Pa-1]
transWSS
0.2
0.0
[Pa]
CFI
0.2
0.0

◀**FIGURE 5. WSS-based descriptors distribution at the luminal surface of the three different types of coronary arteries (LAD, LCX, RCA) from the representative animal model C (see Fig. 2). Red color highlights those areas exposed to low TAWSS, and high OSI, RRT, transWSS and CFI. The very low values of OSI, transWSS and CFI at the luminal surface suggest that WSS is scarcely multidirectional.**

strong association that emerged between RRT66 and TAWSS33 (Table 5), suggesting that RRT was markedly biased by TAWSS. The definition of RRT as a combination of OSI and TAWSS (Table 3), and the very low OSI values characterizing the investigated coronary arteries (Fig. S.6 and Table S.1, Supplemental data), support the observation that RRT66 is a replica of TAWSS33, in the coronary arteries investigated.

As a consequence of the low transWSS values characterizing the hemodynamics of the investigated coronary arteries, and by construction, a significant association emerged between transWSS66 and CFI66 ($r = 0.74$, $p < 0.001$). Interestingly, also a significant association was observed for OSI66 with transWSS66 ($r = 0.59$, $p < 0.001$) and CFI66 ($r = -0.81$, $p < 0.001$).

Furthermore our data showed that larger SAs exposed to low WSS corresponded to smaller SAs exposed to multidirectional WSS, as confirmed by the

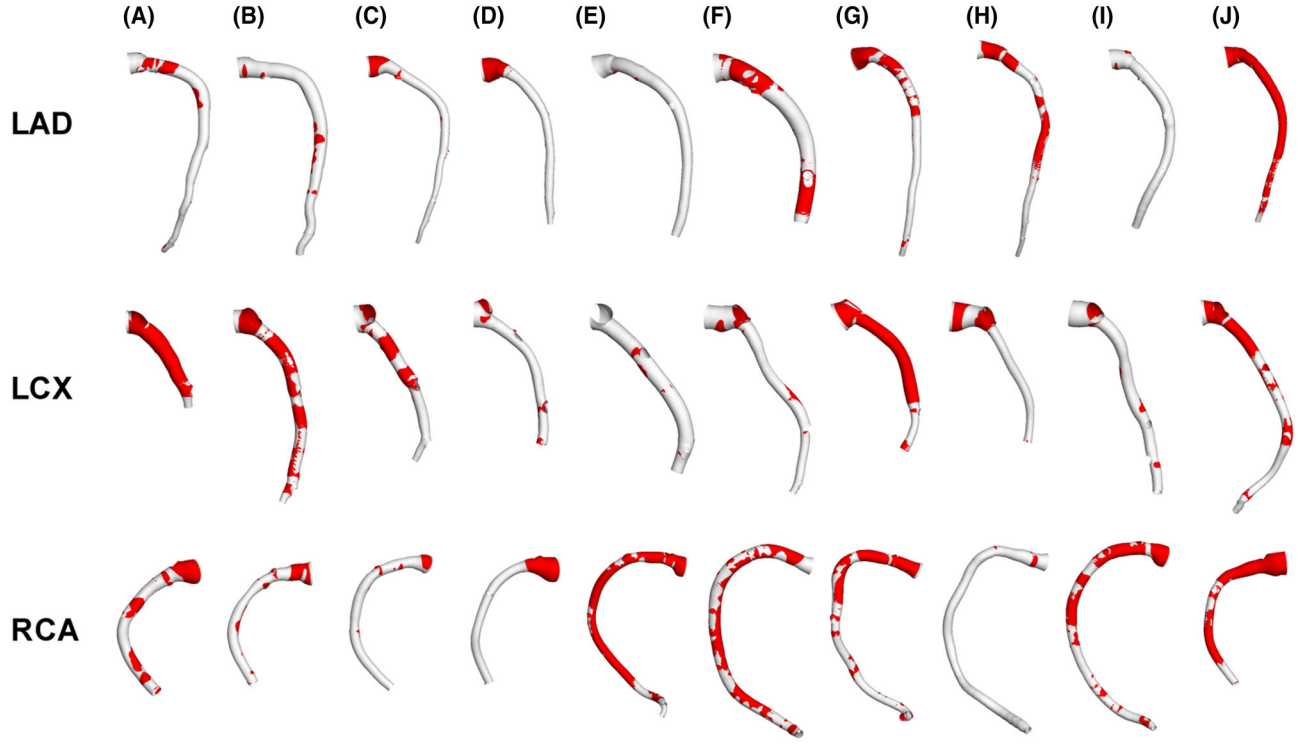

FIGURE 6. Surface areas of the 30 swine coronary artery models exposed to TAWSS33. Labels from A to J identify the single swine model. For each swine, LAD, LCX and RCA geometries were reconstructed. Contour levels for TAWSS33 correspond to lowest tertile value of TAWSS distribution on the combined surface of all models.

TABLE 5. Correlation coefficients between each possible couple of disturbed shear stress parameters (% surface area exposed) and geometry (average curvature and torsion) descriptors.

	%OSI66	%RRT66	%transWSS66	%CFI66	$\bar{\kappa}$	$\bar{\tau}$
%TAWSS33	**− 0.37***	**1.00**‡	**− 0.84***	**− 0.39***	0.12	0.12
	%OSI66	− 0.34	**0.59**‡	**0.81**‡	− 0.28	0.18
		%RRT66	**− 0.83**‡	**− 0.37***	0.13	0.14
			%transWSS66	**0.74**‡	**− 0.37***	− 0.05
				%CFI66	**− 0.49***	0.13
					$\bar{\kappa}$	0.13

Statistically significant values are in bold.
$^{*}p_{value} < 0.05$; $^{\dagger}p_{value} < 0.01$; $^{\ddagger}p_{value} < 0.001$.

moderate negative associations of TAWSS33 with OSI66 ($r = -0.37$, $p < 0.05$), transWSS66 ($r = -0.84$, $p < 0.05$), and CFI66 ($r = -0.39$, $p < 0.05$).

Low and oscillatory WSS areas were neither correlated to curvature nor torsion of the artery (Table 5). Since transWSS66 ($r = -0.37$, $p < 0.05$) and CFI66 ($r = -0.49$, $p < 0.05$) were negatively associated with curvature, our data suggest that curvature in coronary arteries serves to suppress WSS multi-directionality.

Regression analysis revealed significant associations between helicity-based vs. WSS-based descriptors (Table 6). Notably, h_2 was strongly and negatively associated with TAWSS33 ($r = -0.91$, $p < 0.001$), indicating that the higher the h_2 is, the lower the SA of an individual coronary artery exposed to low WSS.

In contrast, positive regression coefficients were found for the significant associations of h_2 with OSI66, CFI66 and transWSS66 (Table 6). For clarity, it must be reported here that the threshold values (66th percentile) identified for OSI (0.002), CFI (0.066) and transWSS (0.039 Pa) are very low in the 30 coronary arteries investigated, suggesting that WSS multidirectionality is not a feature marking out their local hemodynamics (Fig. S.6 and Table S.1, Supplemental data).

TABLE 6. Correlation coefficients for percentage luminal surface areas expose to disturbed shear and helicity-based descriptors and for hemodynamic descriptors vs. geometry (average curvature and torsion).

	h_1	h_2	h_3	h_4
%TAWSS33	**−0.48**†	**−0.91**‡	−0.05	−0.01
%OSI66	**0.50**†	**0.58**‡	**0.39***	0.32
%RRT66	**−0.49***	**−0.90**‡	−0.03	−0.01
%transWSS66	**0.49**†	**0.86**‡	0.13	0.13
%CFI66	**0.47**†	**0.51**†	0.34	0.30
$\bar{\kappa}$	−0.12	−0.22	−0.01	0.11
$\bar{\tau}$	**0.49**†	0.09	**0.64**‡	**0.39***

Statistically significant values are in bold.
$^{*}p_{value} < 0.05$; $^{\dagger}p_{value} < 0.01$; $^{\ddagger}p_{value} < 0.001$.

Associations similar to h_2, although weaker, were observed for h_1 (Table 6). An explanation for this is that overall there is a preferential, even if moderate, cycle-average direction of rotation in the observed bi-helical blood flow patterns establishing in the 30 coronary arteries, as confirmed by the positive sign of average h_3 value and by average h_4 value ($h_4 = 0.112$).

Regarding geometric attributes, Table 6 also shows that neither h_1 nor h_2 were associated with curvature. Torsion was found to be positively correlated with helicity h_1 ($r = 0.49$, $p < 0.01$), with signed (h_3) helical rotation balance ($r = 0.64$, $p < 0.001$), and more weakly with its unsigned (h_4) version ($r = 0.49$, $p < 0.05$), suggesting an important role of vascular torsion in promoting helical flow in coronary arteries.

The nature of the association of h_2 with WSS and geometry can be better appreciated in scatter plots reported in Fig. 7. It emerges that: (1) a non-linear decreasing trend relates h_2 with TAWSS33 (and RRT66 as well), i.e., the percentage SA exposed to low WSS; (2) an almost (positive) linear trend describes the observed association of h_2 with transWSS66; (3) trends in the observed associations are not specific for the different types of coronary arteries.

The observed associations between helicity-based descriptors and percentage of luminal SAs that, based

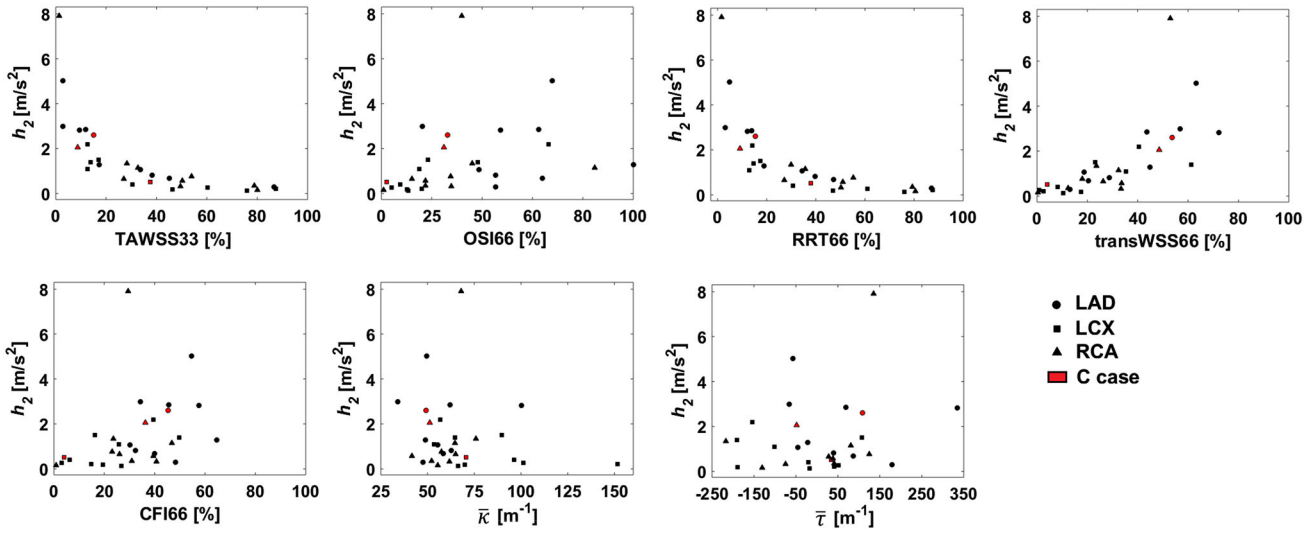

FIGURE 7. Scatter plots of helicity intensity h_2 vs. WSS-based descriptors, and average curvature and values. Red color indicate case C (Fig. 2), used as representative example in Figs. 4 and 5.

on thresholds, are subjected to more 'disturbed shear stress' (Table 6), are confirmed when considering luminal surface area-averaged values of the WSS-based descriptors (Table S.2, Supplemental data).

DISCUSSION

In the last decade quantitative approaches have started to be massively applied to investigate the physiological significance of arterial helical flow. However, despite the qualitatively description of a relationship between helical flow and atheroma formation in coronary arteries,[58] only recently a patient-specific computational study on a small dataset (N = 3) has suggested a link between helical flow and WSS in human coronary artery segments.[69]

Here, the existence of correlations among helical flow, vascular geometry and disturbed shear stress was explored in a representative dataset of 30 swine-specific models of coronary arteries. Among the main findings, it is reported for the first time that distinguishable counter-rotating helical flow patterns were present in all the models under investigation. This suggests that helical flow arrangement is a feature characterizing physiological intravascular hemodynamics in coronary arteries (Fig. 3). Such arrangement in helical structures characterized by high helicity intensity (h_2) stabilizes blood flow imparting low WSS multidirectionality and minimizing the luminal surface exposed to low WSS, thus indicating that helical flow is instrumental in suppressing flow disturbances in coronary arteries. More in detail, since the rotating direction of helical flow patterns dictates the luminal distribution of $\mathbf{WSS}_{sc}$ (Fig. 4, Fig. S.5 in Supplemental data), it emerges that bi-helical flow patterns could influence endothelial shear stress orientation, in coronary arteries. A preferential direction of rotation of the bi-helical flow structures is promoted by vascular torsion, while vascular curvature moderately suppresses an already scarcely multidirectional WSS (Table 5). In fact, very low values of OSI, transWSS and CFI were found (Fig. S.6 and Table S.1, Supplemental data), suggesting a predominant role of low WSS as hemodynamic determinant of plaque formation in coronary arteries. Previous findings support the role of low WSS in promoting endothelial dysfunction,[9,18,61,64,70] although the influence of multidirectional shear stress on endothelial function needs to be investigated more in-depth.

In recent years, computational hemodynamics has made a remarkable contribution to highlight the physiological significance of helical blood flow naturally streaming in arteries. In particular, an *in silico* study on a dataset of 50 models of human carotid bifurcations showed that high helicity intensity is instrumental in suppressing flow disturbances, and thereby is potentially atheroprotective.[19] These findings were supported by the observation that helical flow production in the common carotid artery, reinforcing helicity in the carotid bifurcation, provides further contribution to reduce the likelihood of flow disturbances.[20] Similar findings have been reported using computational fluid dynamics in the healthy aorta, suggesting a key role for helical blood flow in (1) reducing luminal areas exposed to low and oscillatory shear stress,[48] and (2) influencing near-wall transfer of atherogenic particles and oxygen.[36,37] Moreover, computational hemodynamics findings showed that helical blood flow could be posture-dependent.[1] Parallel to basic studies on its physiological significance, the analysis of helical blood flow has been increasingly adopted to better understand how cardiovascular diseases,[11,56,60] or ageing,[16] alter the arterial flow physics.

Several limitations could weaken the findings of this study. Among them, the assumption of rigid vascular wall might have affected TAWSS estimation. However, studies applying fluid-structure interaction approaches reported that TAWSS spatial distribution is preserved using rigid walls.[40] Moreover, the cardiac-induced motion of coronary arteries was neglected. This idealization was based on previous findings demonstrating that myocardial motion has a minor effect on coronary flow and WSS distribution with respect to the blood pressure pulse.[67,73] Moreover, it can markedly affect instantaneous WSS and OSI wall distribution, with minor effects on TAWSS.[68] Therefore, it is expected to have minor impact on the here reported observations.[48] The relatively modest number (N = 30) of coronary artery models investigated could limit the generality of the study. However, the existence of hemodynamic features which are common to all coronary arteries here clearly emerges as the presence of distinguishable helical blood flow patterns, and low WSS multidirectionality. Finally, here swine, not human models, have been used to characterize helical flow in coronary hemodynamics and to investigate whether a causal relationship between helical flow and shear stress exists. However, the close similarity between the human and pig coronary anatomy, in addition to the wide adoption of swine model in studies of coronary disease over the past decades,[72] support the translation of the findings of this study to human coronary arteries. Moreover, helical flow features similar to the ones observed here were reported in a small number of image-based computational hemodynamic models of human coronary arteries,[69] confirming that swine models are representative of the human coronary circulation.

The findings of this study support the future exploration of the links between the observed helical distribution of fatty and fibrous plaques in coronary artery segments and the hemodynamic factors involved in the local onset and progression of atherosclerosis in the coronary tree. In this sense, the present findings will contribute to answer to the still open questions raised since 60 s,[12,13,52,53,58] regarding the observation of irregular spiral distributions of sclerotic bands in coronary arteries.

In conclusion, this study demonstrates that hemodynamics of coronary arteries is characterized by distinguishable and counter-rotating bi-helical flow structures, whose topological features are associated with geometry (in terms of average torsion of the vessel). Remarkably, it emerges that unfavorable conditions of low wall shear stress are strongly and inversely associated with helicity intensity, as already observed in other arterial districts.[19]

ELECTRONIC SUPPLEMENTARY MATERIAL

The online version of this article (https://doi.org/10.1007/s10439-018-02169-x) contains supplementary material, which is available to authorized users.

CONFLICT OF INTEREST

All authors declare that they have no financial and personal relationships with other people or organizations that could have inappropriately influenced the submitted work.

REFERENCES

[1]Aristokleous, N., I. Seimenis, G. C. Georgiou, A. Nicolaides, and A. S. Anayiotos. The effect of head rotation on the geometry and hemodynamics of healthy vertebral arteries. *Ann. Biomed. Eng.* 43(6):1287–1297, 2015.

[2]Arnold, R., M. Neu, D. Hirtler, C. Gimpel, M. Markl, and J. Geiger. Magnetic resonance imaging 4-D flow-based analysis of aortic hemodynamics in Turner syndrome. *Pediatr. Radiol.* 47:382–390, 2017.

[3]Bachler, P., N. Pinochet, J. Sotelo, G. Crelier, P. Irarrazaval, C. Tejos, and S. Uribe. Assessment of normal flow patterns in the pulmonary circulation by using 4D magnetic resonance velocity mapping. *Magn. Reson. Imaging* 31:178–188, 2013.

[4]Bammer, R., T. A. Hope, M. Aksoy, and M. T. Alley. Time-resolved 3D quantitative flow MRI of the major intracranial vessels: initial experience and comparative evaluation at 1.5 T and 3.0 T in combination with parallel imaging. *Magn. Reson. Med.* 57(1):127–140, 2007.

[5]Bogren, H. G., and M. H. Buonocore. Blood flow measurements in the aorta and major arteries with MR velocity mapping. *J. Magn. Reson. Imaging* 4(2):119–130, 1994.

[6]Bogren, H. G., M. H. Buonocore, and R. J. Valente. Four-dimensional magnetic resonance velocity mapping of blood flow patterns in the aorta in patients with atherosclerotic coronary artery disease compared to age-matched normal subjects. *J. Magn. Reson. Imaging* 19:417–427, 2004.

[7]Bogren, H. G., R. H. Mohiaddin, P. J. Kilner, L. I. Jimenez-Borreguero, G. Z. Yang, and D. N. Firmin. Blood flow patterns in the thoracic aorta studied with three-directional MR velocity mapping: the effects of age and coronary artery disease. *J. Magn. Reson. Imaging* 7:784–793, 1997.

[8]Bürk, J., P. Blanke, Z. Stankovic, A. Barker, M. Russe, J. Geiger, A. Frydrychowicz, M. Langer, and M. Markl. Evaluation of 3D blood flow patterns and wall shear stress in the normal and dilated thoracic aorta using flow-sensitive 4D CMR. *J. Cardiovasc. Magn. Reson.* 14(1):84, 2012.

[9]Chatzizisis, Y. S., M. Jonas, A. U. Coskun, R. Beigel, B. V. Stone, C. Maynard, R. G. Gerrity, W. Daley, C. Rogers, E. R. Edelman, C. L. Feldman, and P. H. Stone. Prediction of the localization of high-risk coronary atherosclerotic plaques on the basis of low endothelial shear stress: an intravascular ultrasound and histopathology natural history study. *Circulation* 117:993–1002, 2008.

[10]Chiastra, C., D. Gallo, P. Tasso, F. Iannaccone, F. Migliavacca, J. J. Wentzel, and U. Morbiducci. Healthy and diseased coronary bifurcation geometries influence near-wall and intravascular flow: a computational exploration of the hemodynamic risk. *J. Biomech.* 58:79–88, 2017.

[11]Condemi, F., S. Campisi, M. Viallon, T. Troalen, G. Xuexin, A. J. Barker, M. Markl, P. Croisille, O. Trabelsi, C. Cavinato, A. Duprey, and S. Avril. Fluid- and biomechanical analysis of ascending thoracic aorta aneurysm with concomitant aortic insufficiency. *Ann. Biomed. Eng.* 45(12):2921–2932, 2017.

[12]Fox, B., K. James, B. Morgan, and W. A. Seed. Distribution of fatty and fibrous plaques in young human coronary arteries. *Atherosclerosis* 41:337–347, 1982.

[13]Fox, B., and W. A. Seed. Location of early atheroma in the human coronary arteries. *J. Biomech. Eng.* 103:208–212, 1981.

[14]François, C. J., S. Srinivasan, M. L. Schiebler, S. B. Reeder, E. Niespodzany, B. R. Landgraf, O. Wieben, and A. Frydrychowicz. 4D cardiovascular magnetic resonance velocity mapping of alterations of right heart flow patterns and main pulmonary artery hemodynamics in tetralogy of Fallot. *J. Cardiovasc. Magn. Reson.* 14:16, 2012.

[15]Frazin, L. J., G. Lanza, M. Vonesh, F. Khasho, C. Spitzzeri, S. McGee, D. Mehlman, K. B. Chandran, J. Talano, and D. McPherson. Functional chiral asymmetry in descending thoracic aorta. *Circulation* 82(6):1985–1994, 1990.

[16]Frydrychowicz, A., A. Berger, A. Munoz Del Rio, M. F. Russe, J. Bock, A. Harloff, and M. Markl. Interdependencies of aortic arch secondary flow patterns, geometry, and age analysed by 4-dimensional phase contrast magnetic resonance imaging at 3 Tesla. *Eur. Radiol.* 22(5):1122–1130, 2012.

[17]Frydrychowicz, A., J. T. Winterer, M. Zaitsev, B. Jung, J. Hennig, M. Langer, and M. Markl. Visualization of iliac and proximal femoral artery hemodynamics using time-

resolved 3D phase contrast MRI at 3T. *J. Magn. Reson. Imaging* 25:1085–1092, 2007.
[18]Gallo, D., P. B. Bijari, U. Morbiducci, Y. Qiao, Y. Xie, M. Etesami, D. Haabets, E. G. Lakatta, B. A. Wasserman, and D. A. Steinman. Segment-specific associations between local haemodynamic and imaging markers of early atherosclerosis at the carotid artery: an in vivo human study. *J. R. Soc. Interface* 15:20180352, 2018.
[19]Gallo, D., D. A. Steinman, P. B. Bijari, and U. Morbiducci. Helical flow in carotid bifurcation as surrogate marker of exposure to disturbed shear. *J. Biomech.* 45:2398–2404, 2012.
[20]Gallo, D., D. A. Steinman, and U. Morbiducci. An insight into the mechanistic role of the common carotid artery on the hemodynamics at the carotid bifurcation. *Ann. Biomed. Eng.* 43:68, 2015.
[21]Gallo, D., D. A. Steinman, and U. Morbiducci. Insights into the co-localization of magnitude-based versus direction-based indicators of disturbed shear at the carotid bifurcation. *J. Biomech.* 49(12):2413–2419, 2016.
[22]Garcia, J., A. J. Barker, J. D. Collins, J. C. Carr, and M. Markl. Volumetric quantification of absolute local normalized helicity in patients with bicuspid aortic valve and aortic dilatation. *Magn. Reson. Med.* 78(2):689–701, 2017.
[23]Geiger, J., M. Markl, L. Herzer, D. Hirtler, F. Loeffelbein, B. Stiller, M. Langer, and R. Arnold. Aortic flow patterns in patients with Marfan syndrome assessed by flow-sensitive four-dimensional MRI. *J. Magn. Reson. Imaging* 35:594–600, 2012.
[24]Hansen, K. L., H. Moller-Sorensen, J. Kjaergaard, M. B. Jensen, J. T. Lund, M. M. Pedersen, T. Lange, J. A. Jensen, and M. B. Nielsen. Analysis of systolic backflow and secondary helical blood flow in the ascending aorta using vector flow imaging. *Ultrasound Med. Biol.* 42:899–908, 2016.
[25]Himburg, H. A., D. M. Grzybowski, A. Hazel, J. A. LaMack, X. M. Li, and M. H. Friedman. Spatial comparison between wall shear stress measures and porcine arterial endothelial permeability. *Am. J. Physiol. Heart Circ. Physiol.* 286:H1916–H1922, 2004.
[26]Hope, T. A., and R. J. Herfkens. Imaging of the thoracic aorta with time-resolved three-dimensional phase-contrast MRI: a review. *Semin. Thorac. Cardiovasc. Surg.* 20(4):358–364, 2008.
[27]Hope, M. D., T. A. Hope, S. E. Crook, K. G. Ordovas, T. H. Urbania, M. T. Alley, and C. B. Higgins. 4D flow CMR in assessment of valve-related ascending aortic disease. *JACC Cardiovasc. Imaging* 4(7):781–787, 2011.
[28]Houston, J. G., S. J. Gandy, J. Milne, C. Dick, J. F. Belch, and P. A. Stonebridge. Spiral laminar flow in the abdominal aorta: a predictor of renal impairment deterioration in patients with renal artery stenosis? *Nephrol. Dial. Transplant.* 19:1786–1791, 2004.
[29]Houston, J. G., S. J. Gandy, D. G. Sheppard, J. B. Dick, J. J. Belch, and P. A. Stonebridge. Two-dimensional flow quantitative MRI of aortic arch blood flow patterns: effect of age, sex, and presence of carotid atheromatous disease on prevalence of spiral blood flow. *J. Magn. Reson. Imaging* 18:169–174, 2003.
[30]Huo, Y., and G. S. Kassab. Intraspecific scaling laws of vascular trees. *J. R. Soc. Interface* 9(66):190–200, 2012.
[31]Karino, T. Microscopic structure of disturbed flows in the arterial and venous systems, and its implication in the localization of vascular diseases. *Int. Angiol.* 5:297–313, 1986.
[32]Kilner, P. J., G. Z. Yang, R. H. Mohiaddin, D. N. Firmin, and D. B. Longmore. Helical and retrograde secondary flow patterns in the aortic arch studied by three-directional magnetic resonance velocity mapping. *Circulation* 88:2235–2247, 1993.
[33]Knobloch, V., P. Boesige, and S. Kozerke. Sparsity transform k-t principal component analysis for accelerating cine three-dimensional flow measurements. *Magn. Reson. Med.* 70:53–63, 2013.
[34]Ku, D. N., and D. P. Giddens. Laser Doppler anemometer measurements of pulsatile flow in a model carotid bifurcation. *J. Biomech.* 20(4):407–421, 1987.
[35]Ku, D. N., D. P. Giddens, D. J. Phillips, and D. E. Strandness, Jr. Hemodynamics of the normal human carotid bifurcation: in vitro and in vivo studies. *Ultrasound Med. Biol.* 11(1):13–26, 1985.
[36]Liu, X., Y. Fan, and X. Deng. Effect of spiral flow on the transport of oxygen in the aorta: a numerical study. *Ann. Biomed. Eng.* 38(3):917–926, 2010.
[37]Liu, X., F. Pu, Y. Fan, X. Deng, D. Li, and S. Li. A numerical study on the flow of blood and the transport of LDL in the human aorta: the physiological significance of the helical flow in the aortic arch. *Am. J. Physiol. Heart Circ. Physiol.* 297(1):H163–H170, 2009.
[38]Liu, X., A. Sun, Y. Fan, and X. Deng. Physiological significance of helical flow in the arterial system and its potential clinical applications. *Ann. Biomed. Eng.* 43(1):3–15, 2015.
[39]Malek, A. M., S. L. Alper, and S. Izumo. Hemodynamic shear stress and its role in atherosclerosis. *JAMA* 282(21):2035–2042, 1999.
[40]Malvè, M., A. García, J. Ohayon, and M. A. Martínez. Unsteady blood flow and mass transfer of a human left coronary artery bifurcation: FSI vs CFD. *Int. Commun. Heat Mass Transf.* 39:745–751, 2012.
[41]Markl, M., M. T. Draney, M. D. Hope, J. M. Levin, F. P. Chan, M. T. Alley, N. J. Pelc, and R. J. Herfkens. Time-resolved 3-dimensional velocity mapping in the thoracic aorta: visualization of 3-directional blood flow patterns in healthy volunteers and patients. *J. Comput. Assist. Tomogr.* 28:459–468, 2005.
[42]Markl, M., F. Wegent, T. Zech, S. Bauer, C. Strecker, M. Schumacher, C. Weiller, J. Hennig, and A. Harloff. In vivo wall shear stress distribution in the carotid artery: effect of bifurcation geometry, internal carotid artery stenosis, and recanalization therapy. *Circ. Cardiovasc. Imaging* 3:647–655, 2010.
[43]Meckel, S., L. Leitner, L. H. Bonati, F. Santini, T. Schubert, A. F. Stalder, P. Lyrer, M. Markl, and S. G. Wetzel. Intracranial artery velocity measurement using 4D PC MRI at 3 T: comparison with transcranial ultrasound techniques and 2D PC MRI. *Neuroradiology* 55(4):389–398, 2013.
[44]Moffatt, H. K., and A. Tsinober. Helicity in laminar and turbulent flow. *Ann. Rev. Fluid Mech.* 24:281–312, 1992.
[45]Mohamied, Y., S. J. Sherwin, and P. D. Weinberg. Understanding the fluid mechanics behind transverse wall shear stress. *J. Biomech.* 50:102–109, 2017.
[46]Morbiducci, U., D. Gallo, S. Cristofanelli, R. Ponzini, M. A. Deriu, G. Rizzo, and D. A. Steinman. A rational approach to defining principal axes of multidirectional wall shear stress in realistic vascular geometries, with application to the study of the influence of helical flow on wall shear stress directionality in aorta. *J. Biomech.* 48(6):899–906, 2015.

[47]Morbiducci, U., A. M. Kok, B. R. Kwak, P. H. Stone, D. A. Steinman, and J. J. Wentzel. Atherosclerosis at arterial bifurcations: evidence for the role of haemodynamics and geometry. *Thromb. Haemost*. 115(3):484–492, 2016.
[48]Morbiducci, U., R. Ponzini, D. Gallo, C. Bignardi, and G. Rizzo. Inflow boundary conditions for image-based computational hemodynamics: impact of idealized versus measured velocity profiles in the human aorta. *J. Biomech*. 46:102–109, 2013.
[49]Morbiducci, U., R. Ponzini, M. Grigioni, and A. Redaelli. Helical flow as fluid dynamic signature for atherogenesis in aortocoronary bypass. A numeric study. *J. Biomech*. 40:519–534, 2007.
[50]Morbiducci, U., R. Ponzini, G. Rizzo, M. Cadioli, A. Esposito, F. De Cobelli, A. Del Maschio, F. M. Montevecchi, and A. Redaelli. In vivo quantification of helical blood flow in human aorta by time-resolved three-dimensional cine phase contrast MRI. *Ann. Biomed. Eng*. 37:516–531, 2009.
[51]Morbiducci, U., R. Ponzini, G. Rizzo, M. Cadioli, A. Esposito, F. M. Montevecchi, and A. Redaelli. Mechanistic insight into the physiological relevance of helical blood flow in the human aorta. An in vivo study. *Biomech. Model. Mechanobiol*. 10:339–355, 2011.
[52]Nakashima, T., Y. Iwanaga, and Y. Nakaura. Pathologic study of hypertensive heart. *Acta Pathol. Jpn*. 14(1):129–141, 1964.
[53]Nakashima, T., and T. Tashiro. Early morphologic stage of human coronary atherosclerosis. *Kurume Med. J*. 15(4):235–242, 1968.
[54]National Research Council (US). Committee for the Update of the Guide for Care and Use of Laboratory Animals, Guide for the Care and Use of Laboratory Animals (8th ed.). Washington, DC: National Academies Press (US), 2011.
[55]Peiffer, V., S. J. Sherwin, and P. D. Weinberg. Computation in the rabbit aorta of a new metric—the transverse wall shear stress—to quantify the multidirectional character of disturbed blood flow. *J. Biomech*. 46(15):2651–2658, 2013.
[56]Pirola, S., O. A. Jarral, D. P. O'Regan, G. Asimakopoulos, J. R. Anderson, J. R. Pepper, T. Athanasiou, and X. Y. Xu. Computational study of aortic hemodynamics for patients with an abnormal aortic valve: the importance of secondary flow at the ascending aorta inlet. *APL Bioeng*. 2:026101, 2018.
[57]Ponzini, R., C. Vergara, A. Redaelli, and A. Veneziani. Reliable CFD-based estimation of flow rate in haemodynamics measures. *Ultrasound Med. Biol*. 32(10):1545–1555, 2006.
[58]Sabbah, H. N., F. J. Walburn, and P. D. Stein. Patterns of flow in the left coronary artery. *J. Biomech. Eng*. 106(3):272–279, 1984.
[59]Schaap, M., L. Neefjes, C. Metz, A. van der Giessen, A. Weustink, N. Mollet, J. J. Wentzel, T. W. van Walsum, and W. Niessen. Coronary lumen segmentation using graph cuts and robust kernel regression. *Inf. Process. Med. Imaging* 21:528–539, 2009.
[60]Schäfer, M., A. J. Barker, V. Kheyfets, K. R. Stenmark, J. Crapo, M. E. Yeager, U. Truong, J. K. Buckner, B. E. Fenster, and K. S. Hunter. Helicity and vorticity of pulmonary arterial flow in patients with pulmonary hypertension: quantitative analysis of flow formations. *J. Am. Heart Assoc*. 6(12):e007010, 2017.
[61]Siasos, G., J. D. Sara, M. Zaromytidou, K. H. Park, A. U. Coskun, L. O. Lerman, E. Oikonomou, C. C. Maynard, D. Fotiadis, K. Stefanou, M. Papafaklis, L. Michalis, C. Feldman, A. Lerman, and P. H. Stone. Local low shear stress and endothelial dysfunction in patients with nonobstructive coronary atherosclerosis. *J. Am. Coll. Cardiol*. 71:2092–2102, 2018.
[62]Siebes, M., B. J. Verhoeff, M. Meuwissen, R. J. de Winter, A. E. Spaan, and J. J. Piek. Single-wire pressure and flow velocity measurement to quantify coronary stenosis hemodynamics and effects of percutaneous interventions. *Circulation* 109:756–762, 2004.
[63]Sigfridsson, A., S. Petersson, C. J. Carlhäll, and T. Ebbers. Four-dimensional flow MRI using spiral acquisition. *Magn. Reson. Med*. 68:1065–1073, 2012.
[64]Stone, P. H., S. Saito, S. Takahashi, Y. Makita, S. Nakamura, T. Kawasaki, A. Takahashi, T. Katsuki, S. Nakamura, A. Namiki, A. Hirohata, T. Matsumura, S. Yamazaki, H. Yokoi, S. Tanaka, S. Otsuji, F. Yoshimachi, J. Honye, D. Harwood, M. Reitman, A. U. Coskun, M. I. Papafaklis, and C. L. Feldman. Prediction of progression of coronary artery disease and clinical outcomes using vascular profiling of endothelial shear stress and arterial plaque characteristics: The prediction study. *Circulation* 126:172–181, 2012.
[65]Stonebridge, P. A., P. R. Hoskins, P. L. Allan, and J. F. Belch. Spiral laminar flow in vivo. *Clin. Sci. (Lond)* 91(1):17–21, 1996.
[66]Stonebridge, P. A., S. A. Suttie, R. Ross, and J. Dick. Spiral laminar flow: a survey of a three-dimensional arterial flow pattern in a group of volunteers. *Eur. J. Vasc. Endovasc. Surg*. 52(5):674–680, 2016.
[67]Theodorakakos, A., M. Gavaises, A. Andriotis, A. Zifan, P. Liatsis, I. Pantos, E. P. Efstathopoulos, and D. Katritsis. Simulation of cardiac motion on non-Newtonian, pulsating flow development in the human left anterior descending coronary artery. *Phys. Med. Biol*. 53:4875–4892, 2008.
[68]Torii, R., J. Keegan, N. B. Wood, A. W. Dowsey, A. D. Hughes, G. Z. Yang, D. N. Firmin, S. A. Thom, and X. Y. Xu. MR image-based geometric and hemodynamic investigation of the right coronary artery with dynamic vessel motion. *Ann. Biomed. Eng*. 38:2606–2620, 2010.
[69]Vorobtsova, N., C. Chiastra, M. A. Stremler, D. C. Sane, F. Migliavacca, and P. Vlachos. Effects of vessel tortuosity on coronary hemodynamics: an idealized and patient-specific computational study. *Ann. Biomed. Eng*. 44(7):2228–2239, 2016.
[70]Wentzel, J. J., Y. S. Chatzizisis, F. J. Gijsen, G. D. Giannoglou, C. L. Feldman, and P. H. Stone. Endothelial shear stress in the evolution of coronary atherosclerotic plaque and vascular remodelling: current understanding and remaining questions. *Cardiovasc. Res*. 96(2):234–243, 2012.
[71]Wetzel, S., S. Meckel, A. Frydrychowicz, L. Bonati, E. W. Radue, K. Scheffler, J. Hennig, and M. Markl. In vivo assessment and visualization of intracranial arterial hemodynamics with flow-sensitized 4D MR imaging at 3T. *AJNR Am. J. Neuroradiol*. 28(3):433–438, 2007.
[72]Winkel, L. C., A. Hoogendoorn, R. Xing, J. J. Wentzel, and K. Van der Heiden. Animal models of surgically manipulated flow velocities to study shear stress-induced atherosclerosis. *Atherosclerosis* 241:100–110, 2015.
[73]Zeng, D., Z. Ding, M. H. Friedman, and C. R. Ethier. Effects of cardiac motion on right coronary artery hemodynamics. *Ann. Biomed. Eng*. 31:420–429, 2003.